
Article:
Morris, Stuart, Robinson, A. and Ridgers, Christopher Paul orcid.org/0000-0002-4078-0887 (2021) Highly efficient conversion of laser energy to hard x-rays in high-intensity laser–solid simulations. Physics of Plasmas. pp. 1-12. ISSN: 1089-7674

https://doi.org/10.1063/5.0055398

Physics of Plasmas

Highly efficient conversion of laser energy to hard x-rays in high-intensity laser–solid simulations

Cite as: Phys. Plasmas **28**, 103304 (2021); https://doi.org/10.1063/5.0055398
Submitted: 28 April 2021 • Accepted: 01 October 2021 • Published Online: 19 October 2021

S. Morris, A. Robinson and C. Ridgers

Physics of Plasmas ARTICLE scitation.org/journal/php

Highly efficient conversion of laser energy to hard x-rays in high-intensity laser–solid simulations

Cite as: Phys. Plasmas **28**, 103304 (2021); doi: 10.1063/5.0055398
Submitted: 28 April 2021 · Accepted: 1 October 2021 ·
Published Online: 19 October 2021

S. Morris,[1,a)] A. Robinson,[2] and C. Ridgers[1]

AFFILIATIONS

[1]York Plasma Institute, University of York, Heslington YO10 5DQ, United Kingdom
[2]Central Laser Facility, Rutherford-Appleton Laboratory, Chilton, Didcot OX11 0QX, United Kingdom

[a)]Author to whom correspondence should be addressed: sjm630@york.ac.uk

ABSTRACT

We present simulations, which predict significantly higher laser to x-ray efficiencies than those previously found in high-intensity (10^{20}–10^{22} W cm^{-2}) laser–solid simulations. The bremsstrahlung emission is shown to last for 10–100 ps, which is difficult to model with conventional particle-in-cell (PIC) codes. The importance of collective effects is also demonstrated, showing the limitations of Monte Carlo modeling in these systems. A new, open-source hybrid-PIC code with bremsstrahlung routines has been developed to model this x-ray production in 3D. Special boundary conditions are used to emulate complex electron refluxing behavior, which has been characterized in 1D and 2D full-PIC simulations. The peak x-ray efficiency was recorded in thick gold targets, with (7.4 ± 1.0)% conversion of laser energy into x-rays of energy 1 MeV or higher. The target size is shown to play a role in the conversion efficiency and angular distribution of emitted x-rays, and a simple analytic model is presented for estimating these efficiencies.

I. INTRODUCTION

When a high-intensity laser pulse strikes a solid target, the illuminated surface is ionized and forms a plasma layer. This plasma is further heated by the laser, injecting a large current of high-energy (hot) electrons into the solid, with a roughly exponential energy distribution.[1] Multi-petawatt laser facilities such as ELI[2] and Apollon[3] are expected to reach intensities between 10^{22} and 10^{23} W cm^{-2}, creating hot electrons over 100 MeV in energy. Such electrons could lead to efficient x-ray generation through either nonlinear Compton scatter (NCS) in the laser focus, or through bremsstrahlung as the electrons traverse the solid. These x-rays could act as a source for photonuclear reactions,[4] radiotherapy,[5] radiography,[6] or in pair production for laboratory astrophysics.[7] As x-rays are emitted in the direction of motion for ultra-relativistic particles, angular distributions may also act as a diagnostic for electron motion and divergence within the solid.

Calculating the conversion efficiency of hot electron energy into bremsstrahlung radiation is complicated by the existence of competing energy loss mechanisms. Some energy goes to ionization energy loss, where hot electrons excite atomic electrons in the solid and raise the target temperature. The hot electron current will also draw a resistive return current response, establishing fields, which reduce the hot electron energy and further heat the target (Ohmic heating). Upon reaching the target edge, the highest energy electrons will escape, but the build-up of negative charge beyond the target boundary forms a sheath field, which reflects most electrons back in.[8] Electron refluxing provides an additional energy loss mechanism, as energy may be transferred to ion acceleration, and the sheath field strength can change during a reflux event.[9,10] These processes reduce the energy available for bremsstrahlung radiation and must be characterized.

Several groups have already characterized the x-ray emission in laser–solid simulations by adding bremsstrahlung radiation to particle-in-cell (PIC) codes, and treating the solid as a cold, dense plasma.[11–18] This approach has the advantage of directly modeling the absorption of laser energy in the pre-plasma, but requires a large number of computational macro-particles to suppress self-heating.[16,19] In low-resolution PIC simulations, electrons gain energy non-physically and bremsstrahlung routines allow this energy to be radiated away, producing a false x-ray emission. Due to high computational demands, these codes are typically restricted to short-pulse 2D simulations for thin targets and are often not run long enough to capture the full bremsstrahlung emission. Previous attempts[14,15] to characterize the bremsstrahlung efficiency with PIC codes have considered the energy radiated in 36 and 300 fs, but these run-times are insufficient to capture an emission on the order 10–100 ps.

Other groups[8,20–22] have used Monte Carlo codes like `Geant4`[23–25] to model x-ray production in these systems. Electron injection

characteristics are either modeled with PIC codes or assumed from the laser intensity, duration, and focal spot size, and the bremsstrahlung emission is recorded as electrons propagate through the solid. Cross sections for bremsstrahlung, elastic scatter, and ionization energy loss are evaluated using the known values for electrons in solids, but each electron is treated independently and collective effects such as sheath-field energy loss, resistive electric fields, and any generated magnetic fields are neglected.

We have developed a hybrid extension[26] to the PIC code EPOCH,[19,27,28] including resistive fields and elastic scatter equations,[29,30] with additional bremsstrahlung and Möller scatter algorithms adapted from `Geant4`.[23–25] This provides a similar functionality to the hybrid-PIC code LSP,[31] but in an open-source format. A brief discussion of the code is presented in Sec. II, with technical details and benchmarking covered in the Appendixes. This code has allowed 3D simulation of the full bremsstrahlung emission with some collective effects, which cannot be done using traditional PIC or Monte Carlo codes. The bremsstrahlung radiation characteristics and boundary conditions are presented in Sec. III, where we show significantly higher laser-to-x-ray efficiencies than in previous simulations, which only modeled run-times under 500 fs.[14,15] As the focus of this paper is energy loss within the solid, we will ignore the NCS x-rays associated with electron acceleration in the laser focal spot.[32,33]

II. CODE

A. Hybrid-PIC

Hybrid-PIC codes only simulate the hot electrons in laser–solid interactions, making them far less computationally expensive than traditional full-PIC codes.[29,30] A hybrid field solver assumes the presence of a return current based on the temperature and resistivity of the solid, and adds in the corresponding fields without having to simulate the many cold particles in the solid density plasma. This cold plasma treatment is justified in metals and insulators, as target ionization occurs quickly via pre-pulse heating near the surface, and through Ohmic heating and collisional heating due to hot electron propagation within the target bulk.[34] This hot electron heating will be enough to ensure ionization of the target, providing the injected electron energy is higher than the energy required to ionize most of the target atoms. Equations describing the evolution of the fields, temperature, and resistivity of the solid are presented in Appendix A.

Originally, hybrid-PIC codes were designed to track hot electrons of lower energy than those of interest here, lacking bremsstrahlung radiation and using a continuous form of ionization energy loss.[30] At higher electron energies, a more appropriate form of ionization loss would also include discrete Möller scatter, where incident electrons can lose large amounts of energy creating secondary hot electrons (δ-rays) by fully exciting atomic electrons from the background solid. Algorithms for bremsstrahlung radiation have also been included. The full details of the physics applied to hot electrons as they traverse the solid are given in Appendix B. Additionally, a set of benchmarks for the code is provided in Appendix C.

When hot electrons reach a simulation boundary, those above a critical energy $\kappa_{esc} a_0 m_e c^2$ are removed from the simulation (escaped), while the rest are reflected (refluxed). Here, m_e and c describe the electron rest mass and the speed of light, respectively. The normalized vector potential

$$a_0 \approx 8.5 \times 10^{-6} \sqrt{I_0 \lambda^2}, \tag{1}$$

describes the strength of the laser, with I_0 denoting the peak, cycle-averaged intensity (W m^{-2}), and λ the wavelength. Refluxing electrons have their total momentum reduced by $\kappa_{tnsa} a_0 m_e c$ on each re-injection and are scattered through an angle randomly sampled from a uniform distribution between $\pm 0.5\sigma_{\langle\Delta\theta\rangle}$. The empirical parameters are assigned values $\kappa_{esc} = 2$, $\kappa_{tnsa} = 2.7 \times 10^{-3}$, and $\sigma_{\langle\Delta\theta\rangle} = 23°$. These values were taken from 2D full-PIC simulations of electrons refluxing in sheath fields and are calculated in Sec. III C. A discussion of the uncertainties introduced by simplifying the complex electron reflux behavior into this model is also presented in Sec. IV.

B. Simulation setup

Hybrid-PIC simulations were run to model the hot electron to bremsstrahlung efficiency, $\eta_{e\to\gamma}$ for a variety of targets at different intensities. Unless stated otherwise, the hybrid-PIC simulations in this paper were run with cubic cells of side 0.7 μm, as this was found to be the largest cell size, which converged the electric and magnetic fields in test runs. To improve statistics, the bremsstrahlung cross section was increased by a factor of 10, and macro-photon weights were reduced by the same factor to conserve real particle number. The efficiency of laser energy to hot-electron energy was set to $\eta_{l\to e} = 0.3$.

Hot electrons were injected into the simulation through the x_{min} boundary, with spatial and temporal envelope functions, $f(r)$ and $g(t)$, respectively. A 2D Gaussian was used for $f(r)$, characterized by a radial full-width at half maximum (fwhm), r_{fwhm}. Similarly, a 1D Gaussian was used for $g(t)$, described by the fwhm, t_{fwhm}. To cut off low-weight macro-electrons, nothing was injected when $g(t) < 0.1$, or into cells with $f(r) < 0.5$. This gave a mean envelope of $\langle fg\rangle \approx 0.41$ for cells injecting electrons, with a mean root envelope $\langle\sqrt{fg}\rangle \approx 0.61$.

The laser intensity was varied in the range 10^{20}–10^{22} W cm^{-2}, with $r_{fwhm} = 5\,\mu$m, and $t_{fwhm} = 40$ fs. 1226 macro-electrons per time step were injected into each cell, which satisfied the envelope conditions. Macro-electrons were uniformly injected into a cone where the half angle was the smaller of 20° or $\tan^{-1}(\sqrt{2/(\gamma-1)})$ from Moore scaling,[35] where γ is the Lorentz factor of a given injected electron.

The initial background electron and ion temperatures were set to 300 K. In reality, heating from the rising edge of the main laser pulse would create a complex temperature distribution, but initial target temperatures are unimportant for the evolution of hot electrons due to rapid Ohmic heating. It is expected that the temperature of cells will rise from 300 K to 1 eV in less than 1 fs when exposed to the current density of the injected electron beam, which is a negligible timescale for a 40 fs pulse. In all simulated targets, the injected electron energy is at least 4 times higher than the energy required to ionize a single electron from every target atom, which implies a return current will be present for the hybrid-PIC field solver.[34]

III. RESULTS

A. Bremsstrahlung efficiency

Figure 1 shows $\eta_{e\to\gamma}$ evaluated for multiple $100 \times 100 \times 100$ μm^3 targets in 3D hybrid-PIC simulations. The target materials considered were Al, Cu, Sn, and Au, and plastic CH targets are also shown plotted at atomic number $Z = 2.7$. The peak efficiency of hot electron energy to x-rays over 1 MeV occurs for the 10^{22} W cm^{-2} shot on Au

with $\eta_{e\to\gamma} = 0.25$, which corresponds to a laser to x-ray efficiency of $\eta_{l\to\gamma} = 0.074$.

These simulations consider the full bremsstrahlung emission and observe efficiencies higher than those reported from PIC simulations. Previous estimates[14,15] for $\eta_{l\to\gamma}$ in Al targets at 10^{22} W cm^{-2} have ranged from 4×10^{-6} to 8×10^{-5} compared to 0.014 in these simulations, although the larger target size here also contributes to the greater efficiency. These high efficiencies are significant in experiments where bremsstrahlung is a background, suggesting measurement of x-rays from other processes (e.g., NCS) may be much more difficult than currently expected.

To estimate the run-times required to capture the full bremsstrahlung emission for Fig. 1, the x-ray characteristics were found for different targets shot by a 10^{22} W cm^{-2} pulse. Figure 2 shows the rate of x-ray production for photons over 1 MeV in energy. The emission lasts on the order of 10–100 ps, with a strong dependence on target shape when using reflux boundaries, as electrons in smaller targets spend less time between reflux events and lose energy faster. The emission from lower Z targets lasts longer, as ionization loss and bremsstrahlung have reduced stopping powers. This plot shows x-rays created within the solid and not the x-rays measured outside, as the code lacks target self-attenuation from the photoelectric effect (although this is less important for x-ray energies of a few MeV or greater).

The angular distribution of x-ray energy also varied with target geometry as shown in Fig. 3, although no target reproduced the lobes observed by Vyskočil *et al.*[15] While the data do produce lobes when plotting energy per radian, $dE/d\theta$, in 3D simulations it is more appropriate to plot energy per steradian, $dE/d\Omega$, which re-weights the bins and shows a dominant emission in the forward and backward directions. A novel angular distribution is observed for the small foil 10×50^2 μm^3 target, which shows some emission perpendicular to the injection direction. This is because electrons deflected into the perpendicular direction can travel for a long time and emit many x-rays before hitting another boundary and scattering away. The perpendicular emission is less visible in the large foil 50 μm $\times 1$ mm^2 target as

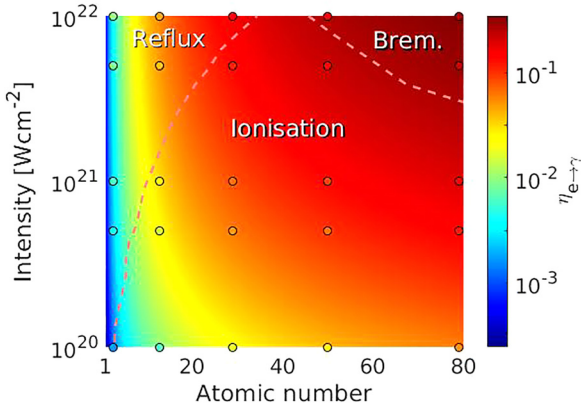

FIG. 1. Efficiency of hot electron kinetic energy to bremsstrahlung x-rays over 1 MeV photon energy in cubic targets of side length 100 μm. The data points show hybrid-PIC simulations, and the background heatmap comes from a simple scaling model. Regions where different energy loss mechanisms dominate are split by the pink lines.

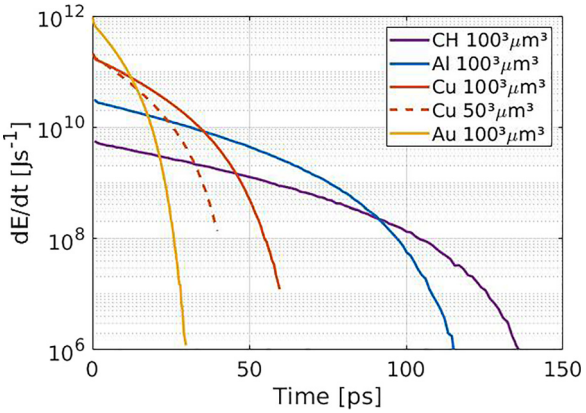

FIG. 2. Temporal distribution of bremsstrahlung radiation from hybrid-PIC simulations, with a laser of intensity 10^{22} W cm^{-2} on cubic targets of various compositions and sizes (labeled l^3 for side length l).

electrons experience reflux scatter less often, and so more energy is lost by the time they scatter into a perpendicular direction.

Figure 3 also shows that magnetic B fields reduce the emission. While B fields cannot take energy from the electrons, it was found that their presence led to more energy loss by resistive fields. This suggests B fields reduce electron divergence, leading to higher current densities and stronger electric fields through (A1).

In Fig. 4, the bremsstrahlung energy spectra are given for some Cu targets. These spectra have a sharp gradient change at $E_\gamma \approx 86$ MeV, as the only electrons, which can radiate above this energy escape the target after only one pass. The size of the target in x determines the length of this pass, and the energy spectra beyond 86 MeV are grouped by this size. Smaller targets produce less bremsstrahlung radiation overall, as reflux events are more common and take away a greater proportion of the hot electron energy.

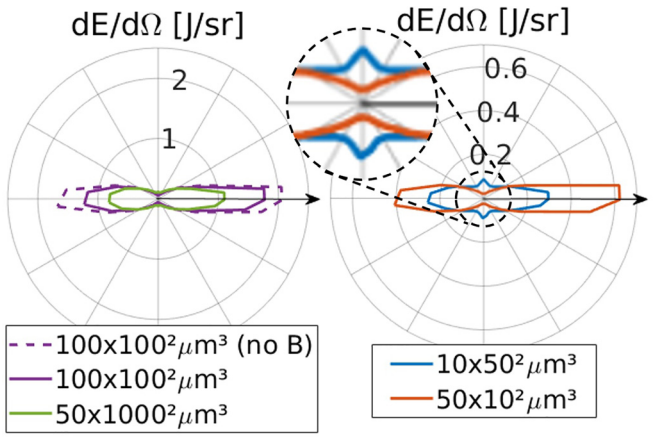

FIG. 3. Angular distribution of bremsstrahlung radiation from hybrid-PIC simulations (10^{22} W cm^{-2}, Cu). The injection direction is given by the arrow, and the sign of p_y determines the deviation direction for the macro-photons. Target dimensions are labeled as $l \times w^2$, where l is the length parallel to electron injection, and the transverse area is $w \times w$. The dashed line data refer to a test where the magnetic field was held at 0 in all cells throughout the simulation.

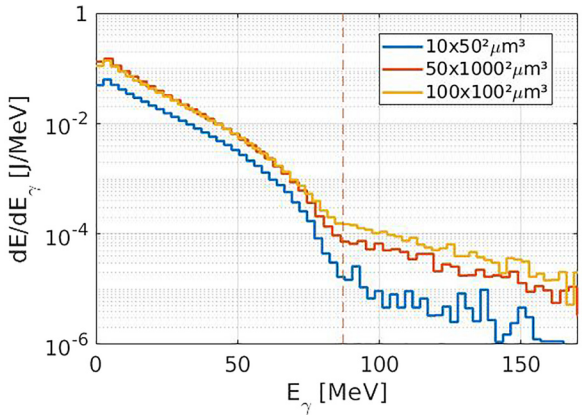

FIG. 4. Photon energy distribution of bremsstrahlung radiation from hybrid-PIC simulations (10^{22} W cm^{-2}, Cu). Target dimensions are labeled as in Fig. 3. The pink line denotes the electron escape energy.

The bremsstrahlung spectrum for the 10×50^2 μm^3 Cu target was also calculated from a simulation without δ-rays. Instead of adding δ-rays as macro-electrons, which can go on to produce photons, their energy was dumped to the local cell as a temperature increase. The resulting spectrum showed no significant difference to the case with δ-rays, which suggests the rare high-energy photon emissions from rare high-energy δ-rays play a negligible role in the total bremsstrahlung emission.

The results presented here rely on boundary conditions, which only approximate the refluxing behavior. Short timescale boundary characterizations (less than 1 ps) were performed in 2D full-PIC codes, although these time-scales were insufficient to model solid decompression. In Al 10^{22} W cm^{-2}, a final background temperature of 3.7 keV was recorded at the focal spot location, which suggests the target could grow 2 μm over 10 ps according to the mean thermal ion speed. The uncertainties introduced by this boundary treatment are addressed in Sec. IV.

B. Energy loss mechanisms

A breakdown of the total energy lost to each mechanism is shown in Fig. 5 for the 10^{20} and 10^{22} W cm^{-2} simulations in 100^3 μm^3 Al and Au targets. It was found that 28% of all lost energy in the Au 10^{22} W cm^{-2} simulation was due to bremsstrahlung radiation (from all photon energies), which dominated all other forms of energy loss. Ionization loss dominated at 10^{20} W cm^{-2}, taking 47% of the hot electron energy in Al and 59% in Au. Reflux energy loss dominated in 10^{22} W cm^{-2} Al, accounting for 51% of the energy loss. Escaping energy took away 17%–22% in all simulations, and resistive fields accounted for 8%–19%. While some electrons gained energy from these electric fields, field gains were less than 2% of the field losses in all four simulations.

A simple model was constructed to quickly estimate the efficiencies of hot electron energy loss mechanisms, and to demonstrate how these scale with laser and target parameters. This model condenses the exponential injection of electron kinetic energies, ϵ_k into three macro-electrons, characterized by the high-energy x-ray threshold, ϵ_γ^{th} (1 MeV here), and the escape energy $\epsilon_{esc} = \kappa_{esc} a_0 m_e c^2$. The "warm"

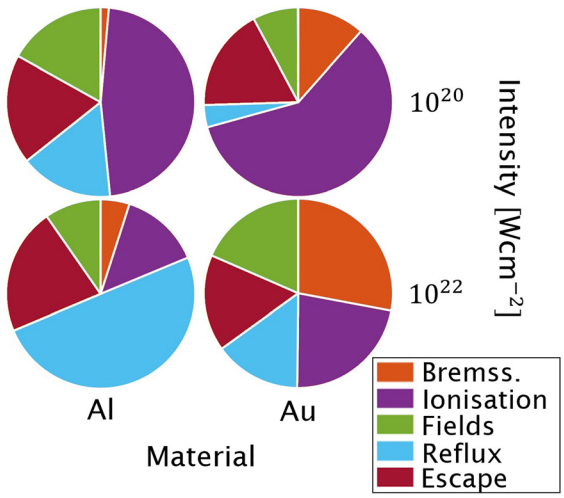

FIG. 5. Hot electron energy loss breakdown for four hybrid-PIC simulations from Fig. 1. The remaining electron energy in these simulations was less than 0.03% of the total energy lost over the runtime.

macro-electron describes all electrons with $\epsilon_k < \epsilon_\gamma^{th}$, the "emitting" macro-electron holds $\epsilon_\gamma^{th} \le \epsilon_k < \epsilon_{esc}$, and the "escaping" macro-electron holds $\epsilon_k \ge \epsilon_{esc}$. The macro-electron weights are found from integrating

$$\frac{dN_e}{d\epsilon_k} = \frac{N_e}{\langle \epsilon_k \rangle} e^{-\epsilon_k/\langle \epsilon_k \rangle}, \tag{2}$$

between the defining kinetic energy limits, where the mean injected kinetic energy $\langle \epsilon_k \rangle = a_0 m_e c^2 \langle \sqrt{fg} \rangle$. From (B1), the total number of injected electrons is

$$N_e = \frac{I_0 \langle fg \rangle \left(\frac{\pi r_{fwhm}^2}{4} \right) \left(t_{fwhm} \sqrt{\frac{\ln 10}{\ln 2}} \right) \eta_{l \to e}}{\langle \epsilon_k \rangle}, \tag{3}$$

after substitution of the full injection area and pulse duration for our envelopes. Similarly, the three macro-electron ϵ_k values are found from integrating $\epsilon_k dN_e/d\epsilon_k$ between the defining energies.

Four stopping-powers are used to characterize energy loss from the individual energy loss mechanisms. For bremsstrahlung[36] and ionization energy loss,[30] we use the continuous stopping power approximations,

$$-\left.\frac{d\epsilon}{dx}\right|_{brem} = \frac{\gamma e^6}{12\pi^3 \epsilon_0^3 m_e c^3 \hbar} n_i Z^2 \ln\left(\frac{5.6\pi\epsilon_0 \hbar c}{Z^{1/3} e^2} \right), \tag{4}$$

$$-\left.\frac{d\epsilon}{dx}\right|_{ion} = \frac{Z n_i e^4}{4\pi\epsilon_0^2 m_e v^2} \left(\ln\left(\frac{\epsilon_k}{I_{ex}} \right) + \frac{1}{2}\ln(\gamma+1) + \frac{0.909}{\gamma^2} - \frac{0.818}{\gamma} - 0.246 \right), \tag{5}$$

where the bremsstrahlung stopping power considers emission into photons of all energies. These use the permittivity of free space, ϵ_0, reduced Planck constant, $\hbar$, and electron charge and speed, e and v, respectively. Solid parameters n_i and I_{ex} denote the ion number density

and mean excitation energy. The stopping power from photons over energy ϵ_γ^{th} is

$$-\frac{d\epsilon}{dx}\Big|_{\epsilon_\gamma>\epsilon_\gamma^{th}} = -\frac{d\epsilon}{dx}\Big|_{brem}\left(\frac{\epsilon_k-\epsilon_\gamma^{th}}{\epsilon_k}\right), \tag{6}$$

which can be used to calculate $\eta_{e\to\gamma}$. In a target of size $L_x \times L_y \times L_z$, the typical path between two boundaries is roughly $(L_x+L_y+L_z)/3$. The energy lost in a reflux event is described by the reflux boundaries, so we approximate a continuous reflux stopping power of the form

$$-\frac{d\epsilon}{dx}\Big|_{tnsa} = \frac{3\kappa_{\mathrm{tnsa}} a_0 m_e c^2}{L_x+L_y+L_z}. \tag{7}$$

For fields, the stopping power is equivalent to the Lorentz force, eE, where the electric fields in this system are described in (A1). Assuming the hot electron current density, j_h is balanced by the background electron current, and the stopping power may be written as $-e\eta j_h$ for a solid with resistivity, η. By approximating a suitable form for $j_h(x)$, we have

$$-\frac{d\epsilon}{dx}\Big|_{field} = e^2\langle\eta\rangle \frac{I_0\langle fg\rangle\left(\frac{1}{2}r_{fwhm}\right)^2 \eta_{l\to e}}{\left(x\tan\theta_c+\frac{1}{2}r_{fwhm}\right)^2\langle\epsilon_k\rangle}, \tag{8}$$

where a constant typical resistivity $\langle\eta\rangle$ has been used. Here, we have assumed the injected current begins with a circular area of radius $r_{fwhm}/2$, where electrons move into a cone of half-angle θ_c, such that the current radius at x includes the $x\tan\theta_c$ term. This ensures the field stopping power diminishes as electrons spread out in the solid.

The warm and "emitting" macro-electrons are integrated through these stopping powers until they have no more energy, and the "escaping" macro-electron is integrated to $x=L_x$, at which point the remaining energy is considered to be escaped. Using $\theta_c = 20^\circ$ and $\langle\eta\rangle = 10^{-6}\Omega$ m, $\eta_{e\to\gamma}$ was calculated over the simulation range shown in Fig. 1 and forms the background heatmap. The $\langle\eta\rangle$ value comes from a simple order-of-magnitude estimate, as resistive fields are only important in the high current densities of the initial injected beam, where temperature and resistivity quickly rise to the order of 100 eV and $10^{-6}\Omega$ m, respectively. This simple model shows good agreement with the simulation data, which supports this choice of $\langle\eta\rangle$.

While calculating this heatmap, a constant $n_i = 6\times10^{28}$ m^{-3} was used, along with the approximation $I_{ex}\approx 11$ eZ. The dominant emission mechanisms were identified in each calculation and are grouped by the pink lines in Fig. 1. For high Z targets, ionization loss dominates at low intensities, while bremsstrahlung dominates at high intensities. In lower Z targets, the stopping power associated with these processes decreases and reflux energy loss becomes the dominant process, making these setups especially unsuitable for modeling using traditional Monte Carlo codes, which lack collective effects.

C. Reflux energy loss

The reflux boundaries described in Sec. II A are characterized by three empirical parameters. These are related to the escape energy threshold, κ_{esc}, the mean reflux momentum loss, κ_{tnsa} and the range of scatter values, $\sigma_{\langle\Delta\theta\rangle}$. The specific values used in the 3D hybrid-PIC simulations of Secs. III A and III B were calculated from 2D full-PIC simulations in EPOCH. These full-PIC runs modeled electron refluxing in the sheath fields and were similar to the characterizations performed by Rusby *et al.*[9]

Four simulations modeled two targets (C and Au) shot at two different laser intensities (10^{20} and 10^{22} W cm^{-2}). All targets were given a pre-plasma for $(-4<x<0)$ μm, with an electron number density $n_e(x) = n_{e0}\exp(x/L_p)$, where n_{e0} is the solid electron number density, and the pre-plasma scale length, $L_p = 2$ μm. The solid density region spanned $0<x<L_s$, where the solid length, and L_s was 10 μm for C and 2 μm for Au. All simulations used a laser with $r_{fwhm} = 5$ μm, and $t_{fwhm} = 40$ fs to match the hybrid-PIC simulations.

C simulations assumed fully ionized targets, with a runtime of 700 fs, 250 macro-electrons, and 50 macro-ions per cell, for square cells of side 20 nm. The simulation window spanned $(-30<x<130)$ μm, with y between ±10 μm. For Au, we used Au^{51+} ions, which had a greater n_e than Al and so smaller square cells of side 5 nm were used to prevent self-heating. The simulation window was reduced to having x and y range between ±10 and ±4 μm, respectively, with 125 macro-electrons and 25 macro-ions per cell, and a run-time of 160 fs.

Simulations were run without collisions for computational efficiency. While this is a poor approximation for the cold background particles, the sheath fields develop according to the hot electron characteristics, which are mostly unaffected by collisions over the considered timescales.[37,38] Using (B4), the time taken for a hot electron of energy $a_0 m_e c^2$ to scatter 90° is at least eight times greater than the simulation run-time in all cases. The energy lost to collisions for this electron is estimated to be under 10% for all simulations according to the collisional stopping power (5).

Six EPOCH particle probes were positioned in the simulation window: two tracking electrons escaping the window through $x_{\min}$ and $x_{\max}$ boundaries, and the rest tracking particles entering and leaving the solid density region at $x=0$ and $x=L_s$. These probes output the momentum, position, and weight of each macro-particle passing them and have been extended to also output particle ID and crossing time. All macro-electrons in the pre-plasma were tracked and were considered hot electrons once they triggered the $x=L_s$ probe for the first time.

Once hot electrons exit the solid-density region there are four possible end-states: re-entering the solid (refluxed), escaping the simulation window through an x boundary (escaped), a y boundary (lost, no useful information), or remaining outside the solid but within the window until the end of the simulation (absorbed into the sheath field). These runs determined the likelihood of these end-states and also looked at how the properties of hot electrons changed over a reflux.

Figure 6 shows a number spectrum of hot electrons in the C 10^{22} W cm^{-2} simulation as they pass $x=L_s$ into the vacuum. Most electrons reflux back into the target, with the highest energy electrons escaping through $x_{\max}$ and some lower energy electrons ending in the sheath field. The κ_{esc} parameter was chosen such that $\kappa_{\mathrm{esc}} a_0 m_e c^2$ was the energy associated with the first bin in Fig. 6, which had all electrons escape after passing into the vacuum from $x=L_s$. The sharp switch of end-states justifies our treatment of a critical escape energy. Electrons labeled as lost have escaped through a y boundary, and it is unclear whether they would have refluxed, escaped, or been absorbed if the simulation window was larger in y.

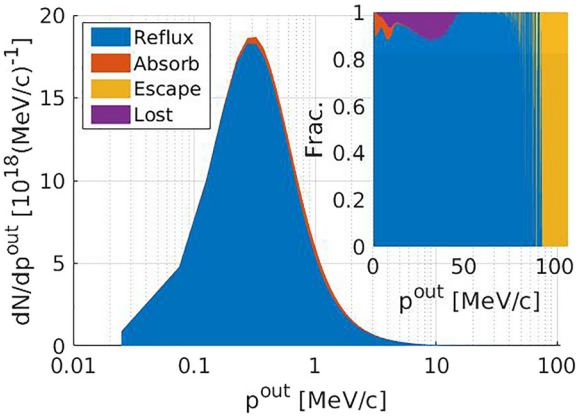

FIG. 6. The number spectrum of hot electrons exiting the solid through $x = L_s$ in the C 10^{22} W cm^{-2} simulation, binned by the electron momentum. The color denotes the distribution of end states in each bin. An inset is provided to show the fate of rare, high-momentum outgoing electrons.

The simulation was repeated with a smaller window of size $(-30 < x < 90)$ μm, and hot electrons were found to escape at the same energy as in the larger window simulations, with similar energy distributions at $x_{\max}$. This suggests convergence in the escape energy cutoff, but these 2D sheath fields will decay slower with distance than fields in 3D space, so this cutoff is likely an over-estimate. The qualitative behavior is similar in all four simulations for electrons exiting through $x = L_s$. Refluxing also dominates electrons exiting the solid on the pre-plasma side through $x = 0$, but the absorption chance is typically greater on this boundary. For example, C 10^{22} W cm^{-2} has 20% absorption in the bin corresponding to the dN/dp peak for the $x = 0$ probe, compared to 2% for the peak bin in the $x = L_s$ probe. However, it is expected that many of these "absorbed" electrons are simply refluxing electrons, which were still outside the solid at the simulation end. A typical reflux event was found to last ~60 fs on the pre-plasma side, but only ~20 fs on the rear, which contributes to the absorption discrepancy between the two sides.

The exiting, p_x^{out}, and returning, p_x^{in}, longitudinal momenta of electrons leaving and reentering the solid through $x = L_s$ was recorded for all reflux events. In Fig. 7, refluxing electrons are binned by p_x^{out} values, and the mean fractional change of longitudinal momentum in each bin is shown by the solid lines for all four simulations. Most hot electrons lose longitudinal momentum when refluxing, with the highest energy electrons losing the most. The κ_{tnsa} parameter is chosen such that $\kappa_{\text{tnsa}} a_0 m_e c$ is the average momentum loss for all hot electrons exiting and reentering the solid, on both the $x = 0$ and $x = L_s$ sides. Electron momenta beyond those plotted in this figure mostly escape the simulation window through the x_{max} boundary. These trends seem similar across the different target materials, sizes, and run-times, although the results appear grouped by intensity.

In C simulations, it was found that $\eta_{l\to e}$ was 0.27 in the 10^{22} W cm^{-2} run, but only 0.03 for 10^{20} W cm^{-2}. This demonstrates different injection characteristics for Fig. 7 simulations and could explain the reduced peak momentum achieved in lower intensity runs (relative to the ponderomotive momentum). The $\eta_{l\to e}$ value for 10^{20} W cm^{-2} is similar to the one found to fit the data for the Fig. 11

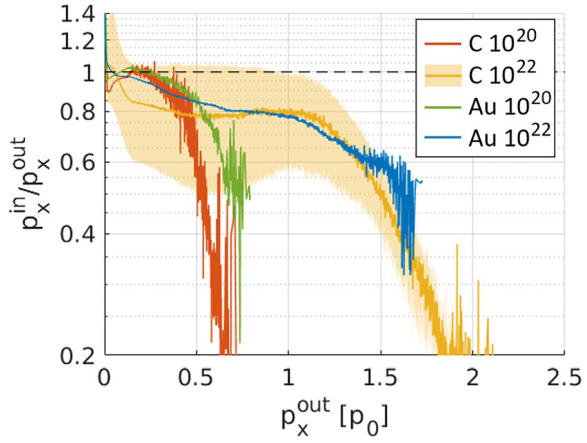

FIG. 7. Refluxing electrons on $x = L_s$ are binned by outgoing longitudinal momentum (in units of the ponderomotive momentum $p_0 = a_0 m_e c$), and the bin averaged momentum change is plotted. Simulations are labeled by target material and laser intensity in W cm^{-2}. The shaded region on C 10^{22} denotes the upper and lower average deviations from the mean in each bin.

benchmark in Appendix C, which was at 3.1×10^{20} W cm^{-2} and also at normal incidence. At oblique incidence, the Fig. 12 benchmark fits with $\eta_{l\to e} = 0.3$, which is closer to that of C 10^{22} W cm^{-2}, despite only being at 4×10^{20} W cm^{-2}. The choice to set $\eta_{l\to e} = 0.3$ in Secs. III A and III B was made to allow for direct comparisons between the results.

In addition to the large decrease in p_x, a smaller increase in p_y was found on refluxing, which contributes to the angle increase observed by Vyskočil *et al.*[15] Figure 8 shows the average change in angle when refluxing for hot electrons exiting the solid at different angles. On average, hot electrons exiting below 30° to the injection direction return at a greater angle, and those above 30° return lower. The shaded region, which denotes average deviation from the mean, is large and roughly uniform over all outgoing angles, which shows a

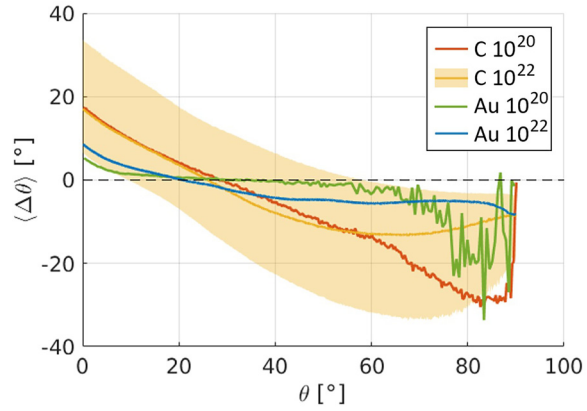

FIG. 8. Refluxing electrons at $x = L_s$ are binned by outgoing $\theta^{\text{out}} = \tan^{-1}(|p_y^{\text{out}}/p_x^{out}|)$, and the $\Delta\theta = \theta^{\text{in}} - \theta^{\text{out}}$ values are averaged in each bin. Simulations are labeled as in Fig. 7. The shaded region for C 10^{22} denotes the upper and lower average deviations from $\langle\Delta\theta\rangle$ in each bin.

large range of scatter angles independent of the outgoing direction. The $\sigma_{\langle\Delta\theta\rangle}$ parameter is the shaded region size for $\langle\Delta\theta\rangle$, averaged over all bins for electron reflux events at both $x = 0$ and $x = L_s$. This average is weighted by the number of electrons in each bin.

The empirical parameters have been calculated in each simulation, and the results are shown in Table I. Typical averages were chosen for κ_{tnsa} and $\sigma_{\langle\Delta\theta\rangle}$ for our hybrid-PIC simulations. We also chose $\kappa_{\text{esc}} = 2$ to be closer to the C 10^{22} W cm^{-2} simulation, as this has the most similar $\eta_{l\to e}$ value to our hybrid electron injection.

IV. DISCUSSION

The boundary conditions of the 3D hybrid-PIC code used an empirical model, which removed high-energy electrons, and reflected the remaining electrons with some energy loss and scatter. This model provides more detail than the reflective boundary conditions typically used in hybrid-PIC codes,[34,39] but relies on 2D full-PIC calculations of electron refluxing in sheath fields. These 2D characterizations had runtimes between 160 and 700 fs, but have been extrapolated to hybrid-PIC simulations, which were run over timescales of 10–100 ps. To test the validity of reflux boundaries over longer timescales, the C 10^{22} W cm^{-2} simulation was repeated in 1D for an extended runtime of 10 ps. The 1D run tested a larger target $L_s = 20\,\mu$m in a simulation window spanning $(-100 < x < 130)\,\mu$m. The cell size was reduced to 10 nm, with 600 macro-electrons and 120 macro-ions per cell. The remaining parameters were set to match those of the 2D simulation. The κ_{tnsa} value from the 1D run was found to be 1.2×10^{-3}, which is comparable to the result found in 2D, although $\sigma_{\langle\Delta\theta\rangle}$ was lower at 9°. This difference in scatter behavior is to be expected, as the transverse electron density profile of the sheath field will play a role in scattering, which is not modeled in 1D. A κ_{esc} parameter cannot be found for the 1D simulation, as no electron energy range had a 100% escape chance, which is attributed to the sheath field strength not decaying over distance in a 1D code.

In the full-PIC simulations, κ_{tnsa} values have been found in the range of $(1.2\text{–}4.2) \times 10^{-3}$, while the results of Sec. III use a typical value of 2.7×10^{-3}. To demonstrate this uncertainty, the simple scaling model of Sec. III B was run over the parameter range shown in Fig. 1, and the lines splitting regions of dominant energy-loss mechanisms have been plotted in Fig. 9 for different κ_{tnsa} values. While there is uncertainty on the reflux-ionization dominance boundary, these results suggest there is still a regime where reflux loss takes a non-negligible fraction of the electron energy. This method has also been used to estimate uncertainties in the x-ray efficiencies found in simulations at 10^{22} W cm^{-2}, with $\eta_{l\to\gamma} = (1.4 \pm 0.7)\%$ for Al, and $(7.4 \pm 1.0)\%$ for Au.

TABLE I. Reflux boundary characterization parameters from 2D full-PIC simulations, labeled by laser intensity in W cm^{-2}, and target material.

	Parameters		
Run	κ_{esc}	κ_{tnsa}	$\sigma_{\langle\Delta\theta\rangle}$ [°]
10^{20}, C	0.81	1.7×10^{-3}	27
10^{20}, Au	0.75	1.6×10^{-3}	10
10^{22}, C	1.9	4.2×10^{-3}	32
10^{22}, Au	1.6	3.2×10^{-3}	22

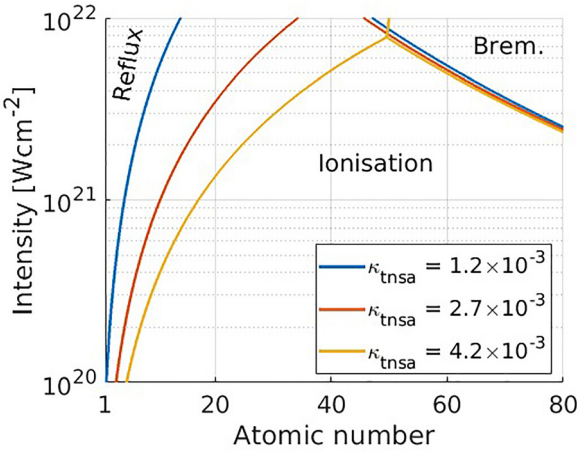

FIG. 9. Separation of the dominant energy loss mechanisms using the simple scaling model. The simulations used the same setup as in Fig. 1, but with the κ_{tnsa} parameter varied between the characterization limits.

The hybrid-PIC code also assumes a general reduced Lee–More model for resistivity calculations, which only offers an approximation to the resistivity profile. Calculations using quantum molecular dynamics (QMD) have demonstrated that the ion structure of the target determines the resistivity behavior, and variations in resistivity model lead to differing electron transport patterns in hybrid-PIC codes.[39] In the case of Si, it was found that the resistivity from an ordered lattice created an electron beam of annular cross-sectional profile, while a disordered lattice led to filamentation in the beam. However, the cross-sectional area of the beam was shown to remain unchanged, so the current density, J, would be similar in all cases. As the resistive electric fields vary with η and J (A1), it is expected that these field strengths will be similar despite the changing electron distributions. Hence, it is expected that field losses will still play an important role as an energy loss mechanism in these systems, although the precise energy loss behavior will depend on the resistivity profile.

V. CONCLUSION

A hybrid-PIC code has been written and benchmarked against experiments for Vulcan shots around 10^{20} W cm^{-2}, where hot electron injection was found to form the dominant source of uncertainty. Full-PIC simulations in 2D demonstrated that over short timescales (up to 700 fs from a 40 fs pulse) most electrons reflux with an energy loss, and the highest energy electrons escape. A table of empirical reflux parameters has been produced, which can be used as a guide to prevent re-characterizing the reflux boundaries for similar experimental setups.

The bremsstrahlung emission occurred over a timescale on the order of 10–100 ps and showed higher efficiencies than previously reported. PIC simulations were shown to underestimate the bremsstrahlung efficiency by orders of magnitude, as they are unable to capture the full emission. Monte Carlo codes are expected to overestimate the emission, as they lack collective energy loss mechanisms. In these 3D simulations, we did not observe the lobes in the bremsstrahlung angular distribution found in 2D full-PIC simulations.

Different energy-loss mechanisms were found to dominate at different laser intensities and target atomic numbers, with bremsstrahlung dominating in high-intensity high-Z setups. A simple analytic model was provided for estimating efficiencies $\eta_{e\to\gamma}$ and showed good agreement with the predictions of the code.

At these timescales, the code could be improved by evolving the immobile background ion fluid with a hydrodynamic code, which could model the effect of hot electrons interacting with laser induced plasma waves within the target. This could be supported by an elastic scatter model, which varied with the target ionization state. Thermal conductivity models could also be added, and simulations could be re-run using target-specific QMD resistivity models. The code could also be extended to include photon transport effects like photoelectric attenuation, and Bethe–Heitler pair production[40] to better model higher intensities.

ACKNOWLEDGMENTS

This work was in part funded by the UK EPSRC Grant Nos. EP/G054950/1, EP/G056803/1, EP/G055165/1, EP/M022463/1, and EP/M018156/1.

The project was undertaken on the Viking Cluster, which is a high-performance compute facility provided by the University of York. We are grateful for computational support from the University of York High Performance Computing service, Viking and the Research Computing team.

We would also like to thank our AWE partners N. Sircombe (now at Arm Ltd.) and G. Crow and for their support in this project.

DATA AVAILABILITY

The data that support the findings of this study (code, input decks, and additional benchmarks) are openly available in the York Research Database at http://doi.org/10.15124/707baa95–44e0–4f55–9476-ef1097b0a668, Ref. 41.

APPENDIX A: SOLIDS

Hybrid-PIC codes model the transport of hot electrons through solids with a significantly colder and denser electron population. The hot electron currents in these systems exceed the Alfvén limit, and propagate by drawing a return current density, $\mathbf{j}_b$, from the background electrons.[42] This return current establishes a resistive electric field, $\mathbf{E}$ according to Ohm's law

$$\mathbf{E} = \eta \mathbf{j}_b, \tag{A1}$$

where η denotes the local resistivity of the solid. To avoid simulation of background particles, the field equations are expressed using only the hot electron current density, $\mathbf{j}_h$, by substituting the total current density $\mathbf{j} = \mathbf{j}_h + \mathbf{j}_b$ into the Ampère-Maxwell law, and iterating the magnetic field $\mathbf{B}$ with the Faraday–Lenz law

$$\mathbf{E} = \eta\left(\frac{1}{\mu_0}\nabla \times \mathbf{B} - \mathbf{j}_h\right), \tag{A2}$$

$$\frac{\partial \mathbf{B}}{\partial t} = -\nabla \times \mathbf{E}. \tag{A3}$$

The displacement current in (A2) has been neglected, as this is negligible over multi-picosecond timescales.[29]

Our code was built as an extension to EPOCH by introducing a new solid concept to the code. Solids are single-element immobile fluids added to the simulation window and are described by an atomic number, Z, mean excitation energy, I_{ex}, and radiation length, X_0. A spatially varying ion number density, $n_{i,}$ is assigned to each solid, and multiple solids may be assigned to the same cell to construct compound materials like plastic.

The hybrid mode also tracks the local background electron and ion temperatures, T_e and T_i (in kelvin) and the resistivity in each cell. The temperature-dependent resistivity is calculated using a reduced form of the Lee–More model,[43]

$$\eta = \frac{m_e}{Z^* n_i e^2 \tau A^\alpha}, \tag{A4}$$

where Z^* is the local solid ionization state (given by the More Table IV algorithm[44]), τ is the electron relaxation time, and A^α is a correction factor. Here, the Lee-More equations have been converted to SI units. Our reduced model varies between the hot and cold relaxation time limits

$$(\tau A^\alpha)_{\text{hot}} = \frac{128\pi\epsilon_0^2}{3e^4}\sqrt{\frac{m_e}{2\pi}}\frac{(k_b T_e)^{3/2}}{(Z^*)^2 n_i \ln\Lambda}, \tag{A5}$$

$$(\tau A^\alpha)_{\text{cold}} = \frac{R_0}{\bar{v}}\lambda_1, \tag{A6}$$

where the Coulomb logarithm $\ln\Lambda$ is evaluated using the Lee–More method,[43] the ion sphere radius $R_0 = (3/4\pi n_i)^{1/3}$, mean thermal speed $\bar{v} = \sqrt{3k_b T_e/m_e}$, and λ_1 is a fitting parameter. The value of τA^α used in (A4) is $\max((\tau A^\alpha)_{\text{hot}}, (\tau A^\alpha)_{\text{cold}})$, and resistivity is taken to be $\eta\lambda_2$, where λ_2 is a second fit parameter. The (λ_1, λ_2) values are taken to be (7) and (3.5) from a fit to experimental Al resistivities.[45]

The electron temperatures of the background solid are updated for each cell and time step according to

$$\Delta T_e = \frac{\rho_\epsilon}{Z n_i C k_b}, \tag{A7}$$

where ρ_ϵ is the density of the energy deposited in the cell over the time step, Δt, and C is the heat capacity[46] of the solid

$$C = 0.3 + 1.2T'\frac{2.2 + T'}{(1.1 + T\prime)^2}, \tag{A8}$$

for $T' = (k_b T_e/e)Z^{-4/3}$. For compound solids, we replace the electron number density term $n_e = Z n_i$ in (A7) with the sum of n_e over all solids in the cell and calculate a cell-averaged $1/C$ value weighted by the n_e value of each solid. This ensures that two overlapping solids of the same material retain the same behavior as the equivalent single solid.

In Ohmic heating, the induced return current dissipates heat by traveling through the resistive solid, depositing an energy density of $\rho_\epsilon = \eta \mathbf{j}_h \cdot \mathbf{j}_h \Delta t$ (as $|\mathbf{j}_h| \approx |\mathbf{j}_b|$).[30] In ionization heating, ρ_ϵ is the sum of the ionization losses for all hot electrons in a cell over Δt, divided by the cell volume.

Background electrons share energy with the ions through collisions, updating the temperatures of each species at the rates

$$\frac{dT_e}{dt} = (T_i - T_e)\frac{(Z^*)^2 e^4 n_i}{t_c}, \tag{A9}$$

$$\frac{dT_i}{dt} = (T_e - T_i)\frac{(Z^*)^3 e^4 n_i}{t_c}, \tag{A10}$$

with the repeated term, t_c representing

$$\frac{1}{t_c} = \frac{2}{3(2\pi k_b)^{3/2}} \frac{\sqrt{m_e m_i}\ln\Lambda}{\epsilon_0^2 (T_e m_i + T_i m_e)^{3/2}}, \tag{A11}$$

where T_i and m_i describe the ion temperature and mass, respectively.[47]

APPENDIX B: HOT ELECTRONS

Hot electrons are injected into the simulation with exponentially distributed energies, and a mean kinetic energy given by ponderomotive scaling, $\langle \epsilon_k(\mathbf{r},t)\rangle = a(\mathbf{r},t) m_e c^2$, for position $\mathbf{r}$ and time t. Here, we use a local normalized vector potential $a(\mathbf{r},t) = a_0\sqrt{f(\mathbf{r})g(t)}$, which applies an intensity reduction to (1) due to the envelope functions $f(\mathbf{r})$ and $g(t)$. The number of electrons injected into the simulation, N_e^{cell}, from a cell with transverse area, A, over a time step, Δt, is given by

$$N_e^{\text{cell}} = \frac{I_0 f(\mathbf{r}) g(t) A \Delta t \eta_{l\to e}}{\langle \epsilon_k(\mathbf{r},t)\rangle}, \tag{B1}$$

where $\eta_{l\to e}$ is the absorption efficiency of laser energy into hot electron kinetic energy.

The ionization energy loss algorithm has been adapted from `Geant4` and takes two forms depending on the energy transferred to background electrons.[23–25] Hot electron energy loss is described by a continuous stopping power when background electrons are excited to energies, ϵ_k^δ, less than a cutoff energy, $\epsilon_{k,\text{cut}}$,

$$\frac{dE}{dx} = \frac{Z n_i e^4}{8\pi\epsilon_0^2 m_e v^2}\left(\ln\left(\frac{2(\gamma+1)m_e^2c^4}{I_{ex}^2}\right) + F^- - \delta\right), \tag{B2}$$

where v and γ are the speed and Lorentz factor of the hot electron, respectively, and $\epsilon_{k,\text{cut}}$ is set to 1 keV. Here, F^- is a function of γ and $\epsilon_{k,\text{cut}}$, and δ is the density effect function.[48] Background electrons excited to energies over $\epsilon_{k,\text{cut}}$ are treated as a discrete emission (δ-rays) and are added into the simulation as macro-electrons.

Secondary particle emission from macro-electrons in a PIC code is achieved using the optical depth method.[49] Over time step dt in a solid with a cross section per atom σ, a macro-electron covers an optical depth, $d\tau = n_i \sigma v dt$, where $d\tau$ is equivalent to the probability of an emission event during dt. The cumulative probability of emission by optical depth τ is $F(\tau) = 1 - e^{-\tau}$. Hence, an optical depth of emission, τ_e, can be sampled for each macro-electron using $\tau_e = -\ln(1 - x_r)$, where x_r is a uniformly distributed random number between 0 and 1. The total τ traversed by a macro-electron is saved, and once this exceeds τ_e a secondary particle is emitted, the saved τ value is reset and a new τ_e is sampled.

Discrete δ-ray emission uses the cross section of high-energy Möller scatter,[48] and a `Geant4` algorithm for sampling the δ-ray energy from the differential cross section.[23–25] A separate optical depth is used for tracking bremsstrahlung photon emission, which is characterized using the Seltzer–Berger differential cross sections.[50] Following the theory of Wu *et al.*,[16] the Seltzer–Berger cross sections are enhanced by the factor, F_σ

$$F_\sigma = 1 + \frac{\ln|\lambda_D/a_s|}{\ln|a_s m_e c^2/\hbar|}\left(\frac{Z^*}{Z}\right)^2, \tag{B3}$$

to account for differences in nuclear charge screening from ionized backgrounds. Here, λ_D is the Debye length of the background ions, and $a_s = 1.4 a_B Z^{-1/3}$ describes charge screening from atomic electrons where a_B denotes the in Bohr radius. The bremsstrahlung photon emission direction is sampled using a `Geant4` algorithm, which draws a direction according to the Tsai differential cross section.[51,52]

Two models for elastic scatter have been implemented: a hybrid-style approach used in previous hybrid-PIC codes[29,30] and a `Geant4`-style approach using an Urban algorithm adapted to the PIC framework.[53] The hybrid model solves the Fokker–Planck equation in the limit of low Z targets and neglects large-angle scattering, deriving an expected deflection, $\Delta\theta$ over time Δt

$$\Delta\theta = \Gamma(t)\sqrt{\frac{Z^2 e^4 n_i \gamma m_e}{2\pi\epsilon_0^2 p^3}\ln\left(\frac{4\epsilon_0 hp}{Z^{1/3} m_e e^2}\right)\Delta t}, \tag{B4}$$

where $\Gamma(t)$ is a random number drawn from a standard normal distribution. The Urban multiple scattering approach uses model functions, which match the angular distribution moments of Lewis theory,[54] and provides an empirical fit for mapping large angle scattering onto experimental results.[55] The full Urban model modifies both angle and position at the end of each step, to account for scattering within the step. Steps within hybrid-PIC simulations are shorter as they are constrained to a single cell, so we neglect the spatial deviation in the PIC implementation.

APPENDIX C: BENCHMARKING

The first benchmark considers the experimental results of Lockwood *et al.*, which measured energy deposition as a function of depth in a variety of targets.[56] In Fig. 10, the hybrid-PIC code attempts to recreate their data for a 0.5 MeV electron beam at normal incidence on a Ta target. This was performed at low electron currents, which give negligible resistive fields, and bremsstrahlung and δ-ray emission may also be neglected at these electron energies. This benchmark mainly tests the ionization energy loss and elastic scatter routines. The 3D simulation window ($x \times y \times z$) spanned $150 \times 2 \times 2$ μm^3 ($256 \times 8 \times 8$ cells), with open boundary conditions in x, and periodic boundaries in y and z. In the first time step, 50 macro-electrons of unit weight were injected into each cell on the $x_{\min}$ boundary, and the simulation ran for 2 ps. The deposited grid energy was deduced from the final electron temperature distribution and the heat capacity used in the simulations, and was summed over all cells which shared an x position. These simulations were performed for both Davies[30] and Urban[23–25] elastic scatter models and show a reasonable agreement with the Lockwood data. As the Davies simulation ran roughly 3 times faster, we have opted for this elastic scatter model in this paper.

The hybrid field solver, Ohmic heating, reduced Lee–More model, and laser-accelerated electron injection were benchmarked against experiments with the Vulcan petawatt laser. Evans *et al.* obtained a temperature-depth curve with data from shots on multiple plastic targets, where the temperature was measured from a

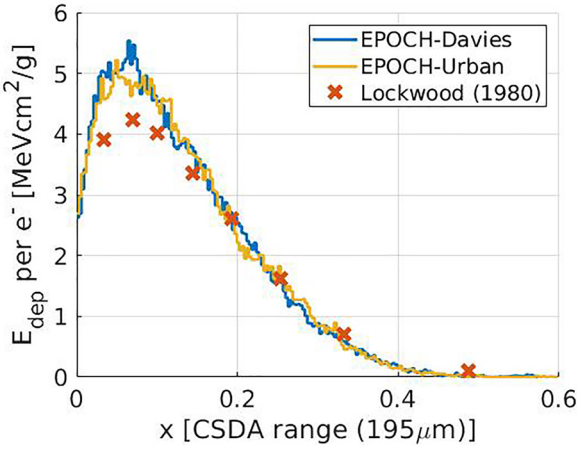

FIG. 10. Energy deposition per incident electron from a 0.5 MeV electron beam injected into a Ta target. Lockwood experimental data are compared to hybrid-PIC simulations running different elastic scatter algorithms.

0.2 μm Al tracer layer buried at different depths.[57] This was recreated in the hybrid-PIC code using a simulation window, which spanned $32.2 \times 20 \times 20$ μm^3 ($322 \times 40 \times 40$ cells), for a target which was Al between $x = 28$ and 28.2 μm, and plastic otherwise. The peak laser intensity was estimated to be 3.1×10^{20} W cm^{-2}, with a temporal fwhm, $t_{fwhm} = 800$ fs, and a spatial radial fwhm, $r_{fwhm} = 10$ μm. To fit the data, we assume $\eta_{l\to e} = 0.04$. To estimate the peak T_e, the slow thermal exchange with ions has been neglected and the final T_e values are recorded at a 1.57 ps snapshot. It was found that there was little change to the central temperatures after this time, as the electron current density had fallen too low for significant Ohmic heating.

The central $T_e(x)$ values are plotted in Fig. 11 and show a reasonable fit to the experimental results. The presence of the Al tracer layer at 28 μm demonstrates the complex target capability of the

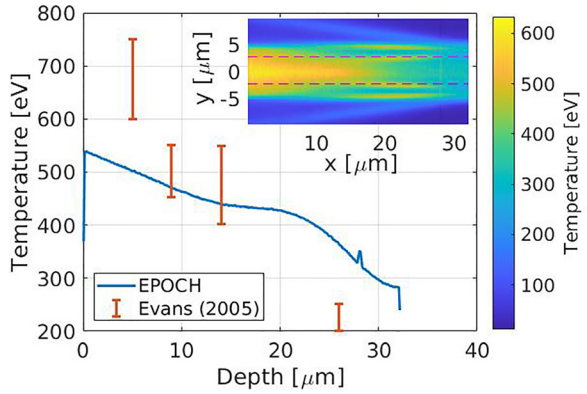

FIG. 11. The temperature distribution of plastic targets with Al tracer layers after exposure to Vulcan shots (3.1×10^{20} W cm^{-2}). Experimental data are compared to the electron temperature from 3D hybrid-PIC simulations, averaged over the central 11×11 cells in y and z for a given x. A 2D heatmap of the temperature averaged over the central 11 cells in z is provided in the inset, where the pink lines denote the central 11 cells in y.

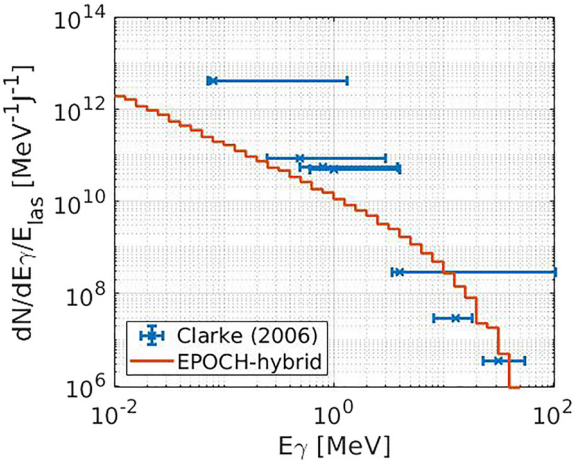

FIG. 12. Number spectrum of x-ray photons from a 4×10^{20} W cm^{-2} shot on a 3 mm Au target, for x-rays falling within a 40° cone (20° half-angle) about the injection direction. Experimental data are compared to an equivalent run using the hybrid-PIC code.

code and shows only a small increase in the temperature at this point. Deviations from experiment are attributed to the rough approximations in the injected electron characteristics, as real injections will be complicated by pre-plasmas and imperfect focal spots.

The final benchmark attempts to recreate the experimental bremsstrahlung photon number spectrum into a 40° forward cone, from 4×10^{20} Wcm^{-2} Vulcan shots on thick Au targets.[58] The code modeled a 3 mm $\times 100^2$ μm^2 Au solid (cubic cells of length 0.7 μm) and captured the full 12 ps emission. Hot electrons were injected with $t_{fwhm} = 800$ fs, $r_{fwhm} = 5$ μm, and $\eta_{l\to e} = 0.3$.

Figure 12 shows the number spectrum of bremsstrahlung photons created with angle less than 20° to the mean injection direction. While we expect to over-estimate the low energy bremsstrahlung emission as our code lacks photoelectric attenuation,[59] we see that low-energy x-rays are actually under-estimated here. When looking at bremsstrahlung x-rays from low current electron beams, the hybrid code matches equivalent runs in `Geant4`, which suggests a correct bremsstrahlung implementation. Hence, the Fig. 12 discrepancy is again attributed to the over-simplified electron injection model.

REFERENCES

[1]T. E. Cowan, M. D. Perry, M. H. Key, T. R. Ditmire, S. P. Hatchett, E. A. Henry, J. D. Moody, M. J. Moran, D. M. Pennington, T. W. Phillips *et al.*, Laser Part. Beams **17**(4), 773–783 (1999).
[2]S. Weber, S. Bechet, S. Borneis, L. Brabec, M. Bučka, E. Chacon-Golcher, M. Ciappina, M. DeMarco, A. Fajstavr, K. Falk *et al.*, Matter Radiat. Extremes **2**(4), 149–176 (2017).
[3]D. N. Papadopoulos, J. P. Zou, C. Le Blanc, L. Ranc, F. Druon, L. Martin, A. Fréneaux, A. Beluze, N. Lebas, M. Chabanis *et al.*, *Conference on Lasers and Electro-Optics (CLEO)* (IEEE, 2019), pp. 1–2.
[4]S. S. Belyshev, A. N. Ermakov, B. S. Ishkhanov, V. V. Khankin, A. S. Kurilik, A. A. Kuznetsov, V. I. Shvedunov, and K. A. Stopani, Nucl. Instrum. Methods Phys. Res., Sect. A **745**, 133–137 (2014).
[5]B. Girolami, B. Larsson, M. Preger, C. Schaerf, and J. Stepanek, Phys. Med. Biol. **41**(9), 1581 (1996).

[6]R. D. Edwards, M. A. Sinclair, T. J. Goldsack, K. Krushelnick, F. N. Beg, E. L. Clark, A. E. Dangor, Z. Najmudin, M. Tatarakis, B. Walton *et al.*, Appl. Phys. Lett. **80**(12), 2129–2131 (2002).
[7]H. Chen, F. Fiuza, A. Link, A. Hazi, M. Hill, D. Hoarty, S. James, S. Kerr, D. D. Meyerhofer, J. Myatt *et al.*, Phys. Rev. Lett. **114**(21), 215001 (2015).
[8]A. Compant La Fontaine, C. Courtois, E. Lefebvre, J. L. Bourgade, O. Landoas, K. Thorp, and C. Stoeckl, Phys. Plasmas **20**(12), 123111 (2013).
[9]D. R. Rusby, C. D. Armstrong, G. G. Scott, M. King, P. McKenna, and D. Neely, High Power Laser Sci. Eng. **7**, e45 (2019).
[10]L. Romagnani, J. Fuchs, M. Borghesi, P. Antici, P. Audebert, F. Ceccherini, T. Cowan, T. Grismayer, S. Kar, A. Macchi *et al.*, Phys. Rev. Lett. **95**(19), 195001 (2005).
[11]Y. Sentoku, K. Mima, T. Taguchi, S. Miyamoto, and Y. Kishimoto, Phys. Plasmas **5**(12), 4366–4372 (1998).
[12]R. Ward and N. J. Sircombe, "Fast particle Bremsstrahlung effects in the PIC code EPOCH: Enhanced diagnostics for laser-solid interaction modeling," Technical Report (AWE, 2014).
[13]R. R. Pandit, Ph.D. thesis, University of Nevada, Reno, 2015.
[14]F. Wan, C. Lv, M. Jia, H. Sang, and B. Xie, Eur. Phys. J. D **71**(9), 236 (2017).
[15]J. Vyskočil, O. Klimo, and S. Weber, Plasma Phys. Controlled Fusion **60**(5), 054013 (2018).
[16]D. Wu, X. T. He, W. Yu, and S. Fritzsche, High Power Laser Sci. **6**, e50 (2018).
[17]B. Martinez, M. Lobet, R. Duclous, E. d'Humières, and L. Gremillet, Phys. Plasmas **26**(10), 103109 (2019).
[18]H. Sawada, Y. Sentoku, A. Bass, B. Griffin, R. Pandit, F. Beg, H. Chen, H. McLean, A. J. Link, P. K. Patel *et al.*, J. Phys. B **48**(22), 224008 (2015).
[19]T. D. Arber, K. Bennett, C. S. Brady, A. Lawrence-Douglas, M. G. Ramsay, N. J. Sircombe, P. Gillies, R. G. Evans, H. Schmitz, A. R. Bell *et al.*, Plasma Phys. Controlled Fusion **57**(11), 113001 (2015).
[20]A. Henderson, E. Liang, N. Riley, P. Yepes, G. Dyer, K. Serratto, and P. Shagin, High Energy Density Phys. **12**, 46–56 (2014).
[21]S. Jiang, A. G. Krygier, D. W. Schumacher, K. U. Akli, and R. R. Freeman, Eur. Phys. J. D **68**(10), 283 (2014).
[22]C. D. Armstrong, C. M. Brenner, C. Jones, D. R. Rusby, Z. E. Davidson, Y. Zhang, J. Wragg, S. Richards, C. Spindloe, P. Oliveira *et al.*, High Power Laser Sci. Eng. **7**, e24 (2019).
[23]S. Agostinelli, J. Allison, K. al Amako, J. Apostolakis, H. Araujo, P. Arce, M. Asai, D. Axen, S. Banerjee, G. Barrand *et al.*, Nucl. Instrum. Methods Phys. Res., Sect. A **506**(3), 250–303 (2003).
[24]J. Allison, K. Amako, J. Apostolakis, H. Araujo, P. A. Dubois, M. Asai, G. Barrand, R. Capra, S. Chauvie, R. Chytracek *et al.*, IEEE Trans. Nucl. Sci. **53**(1), 270–278 (2006).
[25]J. Allison, K. Amako, J. Apostolakis, P. Arce, M. Asai, T. Aso, E. Bagli, A. Bagulya, S. Banerjee, G. Barrand *et al.*, Nucl. Instrum. Methods Phys. Res., Sect. A **835**, 186–225 (2016).
[26]See https://github.com/Status-Mirror/epoch for "Hybrid-PIC Code"
[27]C. P. Ridgers, C. S. Brady, R. Duclous, J. G. Kirk, K. Bennett, T. D. Arber, A. P. L. Robinson, and A. R. Bell, Phys. Rev. Lett. **108**(16), 165006 (2012).
[28]See https://github.com/Warwick-Plasma/epoch for "EPOCH PIC Code"
[29]J. R. Davies, A. R. Bell, M. G. Haines, and S. M. Guerin, Phys. Rev. E **56**(6), 7193 (1997).
[30]J. R. Davies, Phys. Rev. E **65**(2), 026407 (2002).
[31]T. S. Daykin, H. Sawada, Y. Sentoku, F. N. Beg, H. Chen, H. S. McLean, A. J. Link, P. K. Patel, and Y. Ping, Phys. Plasmas **25**(12), 123103 (2018).
[32]K. V. Lezhnin, P. V. Sasorov, G. Korn, and S. V. Bulanov, Phys. Plasmas **25**(12), 123105 (2018).
[33]J. Vyskočil, E. Gelfer, and O. Kilmo, "Inverse compton scattering from solid targets irradiated by ultra-short laser pulses in the 1022-1023 W/cm2 regime," Plasm Phys. Control Fusion **62**, 064002 (2020).
[34]J. R. Davies, A. R. Bell, and M. Tatarakis, Phys. Rev. E **59**(5), 6032 (1999).
[35]C. I. Moore, A. Ting, S. J. McNaught, J. Qiu, H. R. Burris, and P. Sprangle, Phys. Rev. Lett. **82**(8), 1688 (1999).
[36]J. D. Jackson, *Classical Electrodynamics*, 3rd ed. (Wiley, 1998).
[37]S. P. Hatchett, C. G. Brown, T. E. Cowan, E. A. Henry, J. S. Johnson, M. H. Key, J. A. Koch, A. B. Langdon, B. F. Lasinski, R. W. Lee *et al.*, Phys. Plasmas **7**(5), 2076–2082 (2000).
[38]S. C. Wilks, A. B. Langdon, T. E. Cowan, M. Roth, M. Singh, S. Hatchett, M. H. Key, D. Pennington, A. MacKinnon, and R. A. Snavely, Phys. Plasmas **8**(2), 542–549 (2001).
[39]P. McKenna, D. A. MacLellan, N. M. H. Butler, R. J. Dance, R. J. Gray, A. P. L. Robinson, D. Neely, and M. P. Desjarlais, Plasma Phys. Controlled Fusion **57**(6), 064001 (2015).
[40]H. Bethe and W. Heitler, Proc. R. Soc. London, Ser. A **146**(856), 83–112 (1934).
[41]S. Morris, A. Robinson, and C. Ridgers, *Highly Efficient Conversion* of *Laser Energy* to *Hard* X-rays in *High Intensity Laser-Solid Simulations* (University of York, 2021).
[42]D. A. Hammer and N. Rostoker, Phys. Fluids **13**(7), 1831–1850 (1970).
[43]Y. T. Lee and R. M. More, Phys. Fluids **27**(5), 1273–1286 (1984).
[44]R. M. More, Adv. At. Mol. Phys. **21**, 305–356 (1985).
[45]H. M. Milchberg, R. R. Freeman, S. C. Davey, and R. M. More, Phys. Rev. Lett. **61**(20), 2364 (1988).
[46]A. R. Bell, Technical Report No. RL-80-091, 1980.
[47]L. Spitzer, *Physics of Fully Ionized Gases*, 2nd ed (Dover Publications Inc., Mineola, New York, 2006).
[48]H. Messel and D. F. Crawford, *Electron–Photon Shower Distribution Function: Tables for Lead, Copper and Air Absorbers* (Elsevier, 2013).
[49]C. P. Ridgers, J. G. Kirk, R. Duclous, T. G. Blackburn, C. S. Brady, K. Bennett, T. D. Arber, and A. R. Bell, J. Comput. Phys. **260**, 273–285 (2014).
[50]S. M. Seltzer and M. J. Berger, Nucl. Instrum. Methods Phys. Res., Sect. B **12**(1), 95–134 (1985).
[51]Y.-S. Tsai, Rev. Mod. Phys. **46**(4), 815 (1974).
[52]Y.-S. Tsai, Rev. Mod. Phys. **49**(2), 421 (1977).
[53]L. Urbán. Technical Report No. CERN-OPEN-2006-077 (CERN, 2006).
[54]H. W. Lewis, Phys. Rev. **78**(5), 526 (1950).
[55]D. Attwood, P. Bell, S. Bull, T. McMahon, J. Wilson, R. Fernow, P. Gruber, A. Jamdagni, K. Long, E. McKigney *et al.*, Nucl. Instrum. Methods Phys. Res., Sect. B **251**(1), 41–55 (2006).
[56]G. J. Lockwood, L. E. Ruggles, G. H. Miller, and J. A. Halbleib, "Calorimetric measurement of electron energy deposition in extended media. Theory vs experiment," Technical Report No. SAND-79-0414 (Sandia Laboratory, Albuquerque, NM, 1980).
[57]R. G. Evans, E. L. Clark, R. T. Eagleton, A. M. Dunne, R. D. Edwards, W. J. Garbett, T. J. Goldsack, S. James, C. C. Smith, B. R. Thomas *et al.*, Appl. Phys. Lett. **86**(19), 191505 (2005).,
[58]R. J. Clarke, D. Neely, R. D. Edwards, P. N. M. Wright, K. W. D. Ledingham, R. Heathcote, P. McKenna, C. N. Danson, P. A. Brummitt, J. L. Collier *et al.*, J. Radiol. Prot. **26**(3), 277 (2006).
[59]F. Biggs and R. Lighthill, "Analytical approximations for x-ray cross sections III," Technical Report No. SAND-87-0070 (Sandia National Laboratory, Albuquerque, NM, 1988).